Journal of *Marine Science and Engineering*

MDPI

Article

Variation of Semidiurnal Internal Tides along the Southeastern Coast of Korea Induced by Typhoons

Jeong-Yeob Chae [1], Chanhyung Jeon [2], Pyeongjoong Kim [3], Naoki Hirose [4], Ahyoung Ku [1] and Jae-Hun Park [1,*]

[1] Department of Ocean Sciences, Inha University, Incheon 22212, Korea; jychae92@gmail.com (J.-Y.C.); ahyoungku9@gmail.com (A.K.)
[2] Department of Oceanography, Pusan National University, Busan 46241, Korea; chanhyungjeon@gmail.com
[3] Underwater Survey Technology 21 Corp., Incheon 21999, Korea; pjkim@ust21.co.kr
[4] Research Institute for Applied Mechanics, Kyushu University, Fukuoka 816-8580, Japan; hirose@riam.kyushu-u.ac.jp
* Correspondence: jaehunpark@inha.ac.kr; Tel.: +82-32-860-7703

Abstract: Typhoon-induced strong winds can dramatically change the oceanic environment, occasionally resulting in sudden stratification changes. In July 2015, two consecutive typhoons, Chanhom and Nangka, passed over the Yellow and East/Japan Seas within a week. Remarkable temperature variations were observed near the southeastern coast of Korea, caused by typhoon-induced upwelling and downwelling events, which altered the energy of semidiurnal internal tides. During the typhoon-induced downwelling event, the energy of semidiurnal internal tides near the southeastern coast of Korea varied independently from the barotropic tidal forcing. Data-assimilated numerical simulation results reveal that the pycnocline, which is typically tilted toward the coast, enables the semidiurnal internal tidal energy to propagate toward shallow regions after being generated off the coast. Meanwhile, the downwelling event deepens the pycnocline near the coast and reflects and concentrates the semidiurnal internal tide energy near the bottom off the coast. A simple mechanism using the ratio between the wave characteristic slope and the bottom slope is proposed to explain the observed variations of semidiurnal internal tide energy near the coast. This paper demonstrates a case study showing that typhoon passage can modify the energetics of internal tides, which has the potential to cause unusual short-term coastal environmental changes.

Keywords: semidiurnal internal tides; typhoon; southeast coast of Korea; ADCP observation; data-assimilated numerical model

Citation: Chae, J.-Y.; Jeon, C.; Kim, P.; Hirose, N.; Ku, A.; Park, J.-H. Variation of Semidiurnal Internal Tides along the Southeastern Coast of Korea Induced by Typhoons. *J. Mar. Sci. Eng.* **2021**, *9*, 328. https://doi.org/10.3390/jmse9030328

Academic Editor: Wei-Bo Chen

Received: 8 February 2021
Accepted: 13 March 2021
Published: 16 March 2021

1. Introduction

The southeastern coast of Korea is well known for its frequent upwelling events that occasionally last longer than a week during summer months. The water temperature near the coast is sensitive to wind variations; however, the upwelling process is associated with upwelling-favored winds, in addition to the baroclinic structures and bathymetry near the coast [1,2]. Typhoon passages can also be the dominant factor inducing water property changes in coastal regions [3]. Strong cyclonic winds blow around a typhoon and typically create an outward Ekman transport from its center. Considering the southeastern coast of Korea, typhoons passing over the Yellow Sea can create an eastward Ekman transport and typhoons passing over the East/Japan Sea can create a westward Ekman transport, inducing coastal upwelling and downwelling processes, respectively [4,5].

Unexpected temperature variations along coastal areas adversely affect human activities by causing mass mortalities at fish farms under influence of cold-shock stress [6], and efficiency decreases in power plants changing condenser cooling water temperature [7]. The temperature variations over days can be related to the vertical movement of water along coastal areas, caused by upwelling and downwelling processes. In a relatively shorter

time scale, internal waves can cause vertical variations. In particular, internal tides can induce temperature fluctuations with tidal frequencies, because they make water masses move vertically based on tidal periods.

Stratification changes induced by the upwelling and downwelling processes are critical for internal tides as they modify the depth of the pycnocline. Park and Watts [8] showed that the generation and propagation of semidiurnal internal tides at the southwestern corner of the East/Japan Sea changed based on the background current and stratification conditions. Lee et al. [9] explained that the energy generated near the Western Korea Strait propagates near the southeastern coast by using the Regional Oceanic Modeling System. They showed that background stratification changes could modify the internal wave field.

In July 2015, There were two successive typhoons, Chanhom and Nangka, that passed over the Yellow and East/Japan Seas (Figure 1a,b). The two typhoons induced upwelling and downwelling events in series along the eastern coast of Korea [3]. The events made an abrupt 6–8 °C decrease and a consecutive restoration within approximately 5 days, which was recorded near the southeastern coast of Korea using an ocean buoy measuring temperatures at three depths (Figure 1c). A bottom-moored Acoustic Doppler Current Profiler (ADCP) was deployed at a site close to the ocean buoy (Figure 1c) for approximately half a month in July 2015, which overlapped with the period of the two typhoons. The observed current profile timeseries showed energetic tidal frequency fluctuations with abrupt appearances and disappearances, which should be a modulation of internal tides affected by the stratification changes that occurred because of the upwelling and downwelling events.

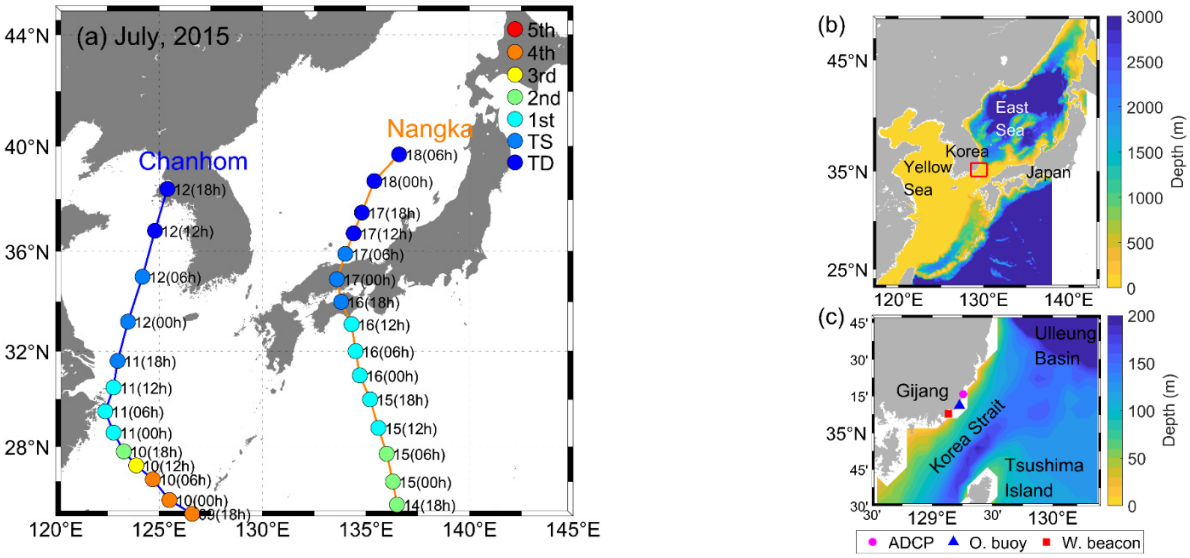

Figure 1. (**a**) Track of the two typhoons, Chanhom and Nangka, around the Korean Peninsula in July 2015. The colors of the circle denote the scale of the typhoon based on the Saffir–Simpson hurricane wind scale, as shown in the top right corner; bathymetry of (**b**) the entire domain of the high-resolution numerical ocean model (DR_M) and (**c**) the southeast coast of Korea. The red square in (**b**) indicates the study area exhibited in (**c**). The magenta, blue, and red markers in (**c**) denote the sites of the Acoustic Doppler Current Profiler (ADCP) mooring, ocean buoy, and wind-measuring light beacon.

In this study, we first show the variations in the observation data and compare them with outputs of the high-resolution numerical ocean model, called DR_M, based on the data-assimilated Research Institute for Applied Mechanics ocean model (RIAMOM) [10]. The whole domain and study area of DR_M is exhibited in Figure 1b,c. Subsequently, typhoon-induced changes in the stratification and the associated variation in semidiurnal internal tides are elucidated using the DR_M outputs. Lastly, dynamical explanations for the variation in semidiurnal internal tides are presented.

2. Data and Methods

Near Gijang, located on the southeastern coast of Korea, a 600-kHz ADCP was moored (~1 km away from the coast) at the bottom from 8 to 24 July 2015 (Figure 1c). The current profiles were recorded in 1 m bins at 10-min intervals together with the bottom temperature. Near-surface data (0–3.6 m depth) were not used in order to avoid undesirable noise. Tidal analyses of the two semidiurnal major tidal constituents (M_2 and S_2) were applied to the data using the T_tide Matlab toolbox [11]. The temperature data at depths of 5, 10, and 15 m could be accessed through an ocean buoy (bgj8a station), which is ~9 km away from the ADCP mooring and located at the water depth of ~20 m. It had been maintained by the National Institute of Fisheries Sciences in Korea, and the data are freely accessible on their website (http://www.nifs.go.kr/risa, accessed on 16 March 2021). Hourly wind data were obtained at a light beacon (Gwangan station) near the mooring. The Korea Meteorological Administration (KMA) provides wind data collected from light beacons through their open data portal service (https://data.kma.go.kr, accessed on 16 March 2021). The observation was conducted at a height of 12 m. The passage and wind speeds of the typhoons were obtained using the Northwestern Pacific Ocean best track data from the Joint Typhoon Warning Center (JTWC). Information regarding the observations and two typhoons used in this study is presented in Tables 1 and 2, respectively.

Table 1. Information regarding observations used in this study.

Site	Latitude	Longitude	Period	Used Data
ADCP mooring	35.264° N	129.258° E	8–24 July 2015	Current profile and bottom temperature
Ocean buoy (bgj8a)	35.187° N	129.227° E	4 November 2008–present	Temperatures at depths of 5, 10, and 15 m
Light beacon (Gwangan)	35.132° N	129.136° E	20 February–6 October 2018	Wind at a height of 12 m

Table 2. Information regarding typhoons Chanhom and Nangka (from the Joint Typhoon Warning Center (JTWC) website https://www.metoc.navy.mil/jtwc, accessed on 16 March 2021).

Name	Date (Birth–Destruction)	Position (Birth–Destruction)	Maximum Sustained Wind Speed (m/s)
Chanhom	30 June–12 July 2015	09° N, 161.4° E–38.4° N, 125.4° E	62
Nangka	3–18 July 2015	8.8° N, 172.2° E–39.7° N, 136.6° E	69

The numerical ocean model analyzed in this study is the East-Asian marginal seas model (DR_M), with resolutions of 1/12° and 1/15° in the zonal and meridional directions, respectively, and 40 vertical levels with an hourly temporal resolution (320 × 384 × 40 grid points) [10]. The output of the Japan Meteorological Agency Meso-Scale Model (JMA/MSM) was obtained at 3 h intervals and used for the meteorological forcing data. Tidal forcings were introduced at the open boundary using the explicit tidal motion of NAO.99jb [12]. DR_M can be visualized on the website with specific information (https://dreams-c2.riam.kyushu-u.ac.jp/vwp/, accessed on 16 March 2021). Studies have focused on the behavior of internal tides using numerical ocean models based on RIAMOM [13–15]. On comparing the observation data and DR_M outputs, the data from model grids closest to the observation points were used. The nearest point to the ADCP mooring site has a depth of 10 m, which is shallower than the actual depth (20.6 m); the selected model grid point for the ocean buoy has a greater depth of 81 m, as compared to the real depth of 20 m.

The buoyancy frequency (N) is defined as $N = \left(-g\,\rho^{-1}\partial\rho/\partial z\right)^{1/2}$, where g is the gravitational acceleration, ρ is the density, and z is the vertical coordinate (positive upward). A 36 h phase-preserving third-order Butterworth low-pass filter was applied to

density in the calculation to exclude tidal signals. Assuming that temperature is a dominant factor in determining density, the vertical displacement (η) was calculated using $\eta = \left(Temp - \overline{Temp}\right) \partial z / \partial Tem$, where $Temp$ is the temperature and $\overline{Temp}$ is the 2-d moving-averaged temperature, used to subtract the non-tidal variations in changing stratification conditions [16].

A phase-preserving third-order Butterworth bandpass filtering was applied to the DR_M outputs and observed ADCP data with cutoffs at 10 and 15 h to extract semidiurnal signals. Hereafter, U and V denote the zonal and meridional currents, respectively, and P represents the pressure; baroclinic components are marked by the subscript "bc" (e.g., U_{bc} Filtered variables, denoted as primed variables ($U_{bc}{}'$, V'_{bc} , P', and $\rho\prime$), are used for several calculations to depict the characteristics of internal tides from the DR_M output. The horizontal kinetic energy (HKE) and available potential energy (APE) were calculated using the following equations:

$$APE = \frac{1}{2T}\left(\int_0^t g^2\, \rho\prime(z,t)^2\, N^{-2}\, \rho(z,t)^{-1} dt\right), \text{ and} \tag{1}$$

$$HKE = \frac{1}{2T}\left(\int_0^t \rho(z,t)\, \left[\, |U_{bc}\prime(z,t)|^2 + |V_{bc}\prime(z,t)|^2 \,\right] dt\right), \tag{2}$$

where t is the time and T is the averaged period. The total energy (TE) is calculated as the sum of the APE and HKE [14,17].

The depth-integrated horizontal energy flux (EF) and barotropic to baroclinic energy conversion rate (E_{bt2bc}) are calculated as

$$EF = \frac{1}{T}\int_0^t \left(\int_{-H}^{\eta} \vec{U_{bc}}\prime P' dz\right) dt, \tag{3}$$

$$E_{bt2bc} = \frac{1}{T}\int_0^t \left(g\int_{-H}^{\eta} \rho' W_{bt} dz\right) dt, \tag{4}$$

$$W_{bt} = \overline{U}\frac{\partial h}{\partial x} + \overline{V}\frac{\partial h}{\partial y} + \frac{\partial \eta}{\partial t'}, \text{and} \tag{5}$$

$$h = H + \eta, \tag{6}$$

where η is the sea level perturbation, h is the total water depth of the column, and $\vec{U_{bc}}\prime$ is the bandpass-filtered baroclinic velocity vector in Cartesian coordinates [14,18].

3. Results and Discussion

3.1. Variations in Wind and Temperature

In a previous study using satellite and ocean buoy data obtained near the eastern coast of Korea, the sudden temperature changes in July 2015 were shown to be caused by typhoon-induced upwelling and downwelling events [3]. The temperatures at depths of 5, 10, and 15 m, obtained from the ocean buoy shown in Figure 2, revealed a consistent decrease and increase in July 2015. Simultaneously, wind data from the nearest light beacon (Figure 2a) showed successive changes from northerly to southerly around 12 July and from southerly to northerly around 15 July, during the passing of the two typhoons.

For comparison, we extracted temperatures at the same depths of 5, 10, and 15 m from the DR_M outputs and the wind input for the model at the grid point nearest to the observation site (Figure 3). The winds used to force the model (Figure 3a) were in good agreement with the observed winds, with root-mean-squared differences (RMSDs) of 3.2 and 2.1 m/s for the zonal and meridional components, respectively. Correspondingly, the temperatures from the ocean buoy and DR_M outputs show similar changes related to the typhoon events, i.e., decreasing during the period of Chanhom (11–13 July) and increasing during the period of Nangka (15–17 July). Owing to the difference in water depths for the ocean buoy (~20 m) and the nearest model grid point (81 m), the simulated

temperature exhibits relatively small changes. Nevertheless, our scope is on the modulation of internal tides associated with the typhoon-induced stratification changes, and hence, the environment with a similar stratification condition can be considered more important.

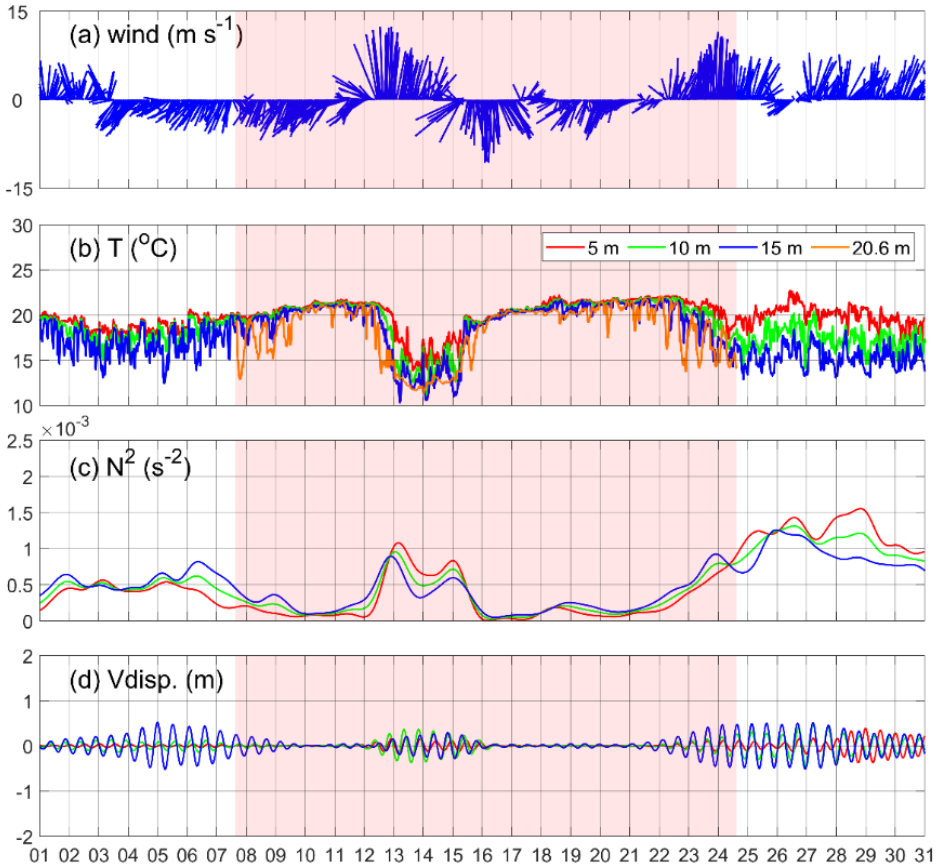

Figure 2. Timeseries of (**a**) 12 m wind speed at the light beacon; timeseries of (**b**) temperature, (**c**) buoyancy frequency, and (**d**) semidiurnal vertical displacement at depths of 5, 10, and 15 m, calculated using ocean buoy data. Red, green, and blue lines denote the depths of 5, 10, and 15 m, respectively. The orange line in (**b**) indicates the bottom temperature at a depth of 20.6 m observed by ADCP mooring, and the reddish highlight denotes the period of the ADCP observation.

The water temperature exhibits a decreasing trend with enhanced stratification (increased N^2), coinciding with the southerly wind. However, as the northerly wind becomes stronger, the temperature reveals an increasing trend with weakening stratification (decreased N^2). The vertical displacement (η) estimated using the temperature changes at different depths shows the signals induced by the semidiurnal internal tides (Figures 2d and 3d). Notably, it follows the trend of N^2 values, which confirms that the stratification condition significantly affects the internal tidal energy in shallow coastal areas. The vertical displacement from the DR_M output also shows a behavior similar to that from the observations. These comparisons support that the DR_M reasonably simulates the stratification changes and η under the influence of the two typhoons.

The horizontal temperature gradient is more apparent in the upper panels of Figure 4, which maps the surface temperature superimposed with the potential density contours and 10-m wind vectors. Daily means of 13 and 17 July are displayed in order to show the typhoon-induced changes clearly, when lower temperature and higher N2 existed during the upwelling event and higher temperature and lower N2 existed during the downwelling event (Figures 2 and 3). The horizontal maps for the monthly mean in July and the daily mean on 13 July indicate that the density contours accumulate near the southeastern coast with upwelled cold waters and southerly winds (Figure 4b). When northerly winds induce

downwelling, the temperature increases near the coast with a decreased horizontal density gradient (Figure 4c). The zonal vertical sections over the ADCP mooring site, with monthly and daily average temperatures and densities, depict the typhoon-induced changes. The monthly mean zonal section shows that the isopycnal surfaces were tilted upward toward the coast in July 2015. The daily average on 13 July, representing the upwelling event, shows that the isopycnal surfaces become steeper, and the horizontal density gradient increases near the coast (Figure 4e). In contrast, the daily average on 17 July, representing the downwelling event, indicates almost flat isopycnal surfaces, with the weakened coastal front (Figure 4f).

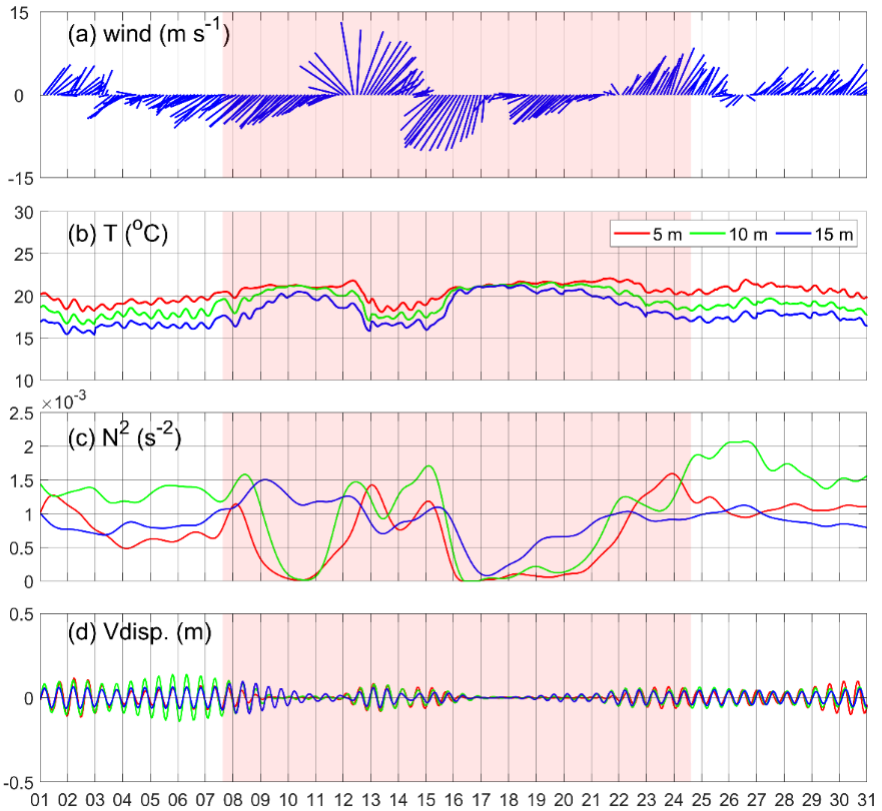

Figure 3. Timeseries of (**a**) 10-m wind from the Japan Meteorological Agency Meso-Scale Model (JMA/MSM) at the grid point of DR_M nearest to the observation site; timeseries of (**b**) temperature, (**c**) buoyancy frequency, and (**d**) semidiurnal vertical displacement at depths of 5, 10, and 15 m, from the nearest grid point of the DR_M, (depth of 81 m) to the ocean buoy (depth of ~20 m). Red, green, and blue lines denote depths of 5, 10, and 15 m, respectively. The reddish highlight denotes the period of the ADCP observation.

3.2. Variations in Current Profiles

Barotropic tidal currents for the two major semidiurnal tidal constituents (M_2 and S_2) were compared between the observed and simulated data (Figure 5 and Table 3). The distance between the nearest grid and the ADCP mooring site is approximately 5 km, and the depth at the nearest grid point is 10 m, which is less than the depth at the mooring site (20.6 m). Nevertheless, the vertical grids are at depths of 1, 3.5, 6.5, and 10 m, enough to simulate the baroclinic processes caused by tides. The distance can also be acceptable when compared with the wavelength of first mode M_2 internal tide, which is 40–100 km in the Southern East/Japan Sea [14]. The M_2 tidal current obtained from the observation and simulation shows similar characteristics, with the RMSD values for the semi-major axis, semi-minor axis, and phases of 0.004 m/s, 0.004 m/s, and 35.6 min, respectively (Table 3). However, the tidal currents from the DR_M outputs are rotated in a clockwise direction when compared to the observed (~31°). This characteristic results in RMSD values of 0.07

and 0.06 m/s for the zonal and meridional semidiurnal tidal currents, respectively. The rotation appears to occur because the grid point is located at a sharp corner of the coastline

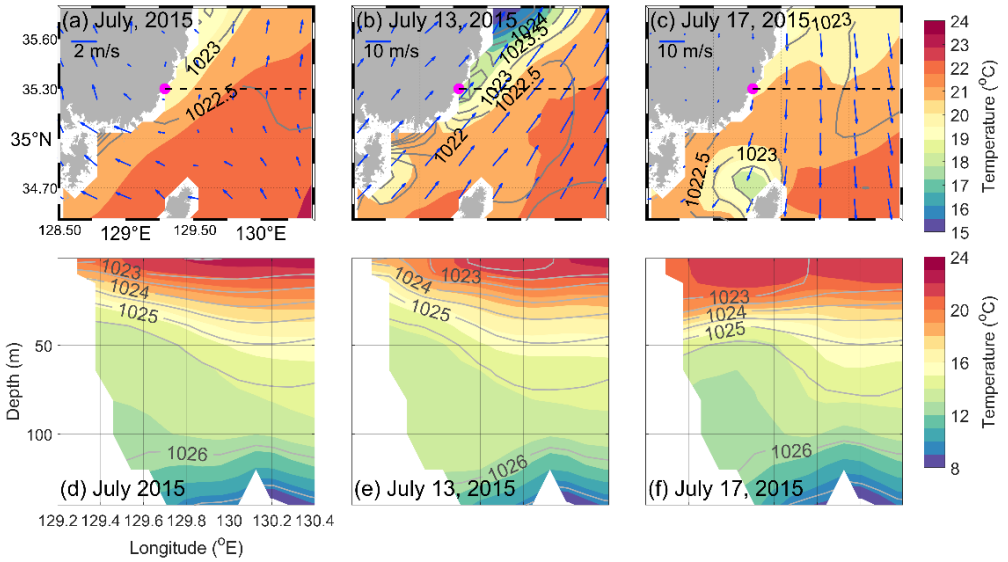

Figure 4. Average sea surface temperature, 10 m winds (arrows), and potential density (grey contours) from the DR_M, (**a**) in July, (**b**) on 13 July, and (**c**) on 17 July 2015; zonal sections for average water temperature and potential density (grey contours) (**d**) in July, (**e**) on 13 July, and (**f**) on 17 July 2015, along the black dotted line in (**a**–**c**). The contour interval of the potential density is 0.5 kg/m^3.

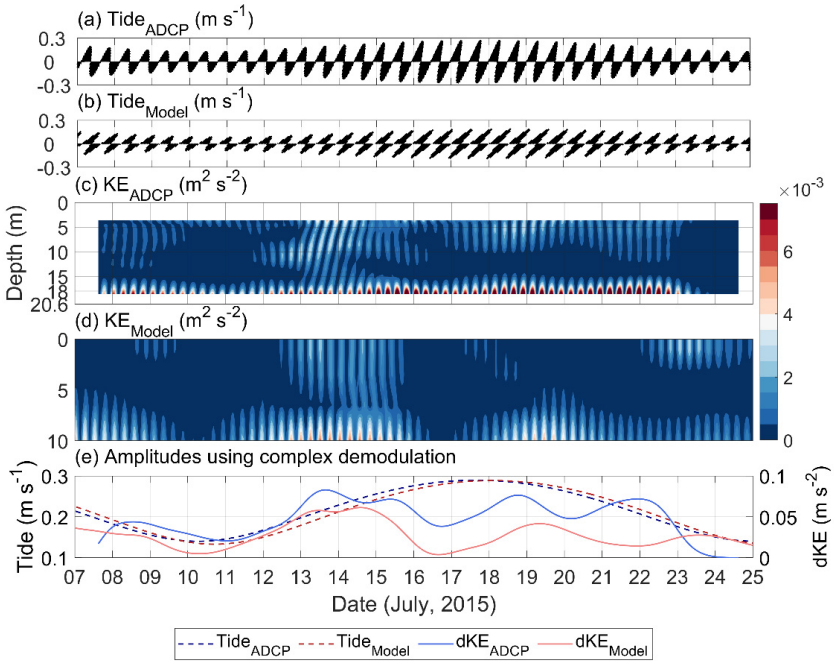

Figure 5. Timeseries of barotropic tide for M_2 and S_2 constituents from (**a**) the ADCP observation and (**b**) the outputs of DR_M; timeseries of kinetic energy for baroclinic semidiurnal currents from (**c**) the ADCP observation and (**d**) the outputs of DR_M. (**e**) Timeseries of amplitudes of barotropic tide for M_2 and S_2 constituents (dashed lines) and depth-integrated kinetic energy for baroclinic semidiurnal currents (solid lines) using complex demodulation from the ADCP observation (blue lines) and the outputs of DR_M (red lines).

Table 3. Tidal ellipse parameters of dominant semidiurnal tidal components for the ADCP observation and DR_M output.

Constituents (ADCP/DR_M)	Semi-Major Axis (m s^{-1})	Semi-Minor Axis (m s^{-1})	Inclination (°)	Phase (°)
M2	0.215/0.211	0.004/0.000	72.9/42.3	47.0/64.3
S2	0.075/0.078	0.003/0.000	72.6/41.8	75.8/103.8

The timeseries of the kinetic energy for baroclinic semidiurnal currents (KE) from the ADCP observation and DR_M output reveals that the energies are high in the upper and lower layers during the upwelling, 12–14 July (Figure 5). However, the energy diminishes with the downwelling event, 16–17 July, when N^2 at the ocean buoy site becomes close to zero (Figures 2 and 3). The energy changes in the ADCP observation is similar to the variation in the semidiurnal vertical displacement at the ocean buoy. To compare the KE with barotropic semidiurnal tides, amplitudes of the depth-integrated KE (dKE) and barotropic tidal currents were calculated using complex demodulation [19] (Figure 5e). The amplitude of dKE is higher in the upwelling period than downwelling period, although the amplitude of tidal currents is weaker. This implies that the internal tidal signal fluctuated independently from the magnitude of the barotropic tides.

At the ADCP mooring site, the semidiurnal KE reveals responses related to the typhoon-induced stratification changes. This result shows that stratification is the dominant factor in determining the energy of internal tides near the coast, acting as their restoring force. Two possible mechanisms can be suggested to explain the existence of internal tidal energy near the coast, i.e., near-field and far-field processes: (1) semidiurnal energy is locally generated and typhoon-induced stratification changes modify the generation process (near-field process); and (2) the observed semidiurnal signal arrives from another source region and is modified by the stratification condition encountered (far-field process). The following sections describe dynamic explanations for the two mechanisms.

3.3. Generation of Semidiurnal Internal Tides

The energy conversion rate from the barotropic to baroclinic tides (E_{bt2bc}) shows where the energetic semidiurnal internal tides can be generated. The map of semidiurnal E_{bt2bc} reveals higher values near Northern Tsushima Island and the southern slope of the Ulleung Basin (Figure 6a). The conversion rate is almost zero near the southeastern coast of Korea, implying that the generation of semidiurnal internal tides are relatively inactive near the coast.

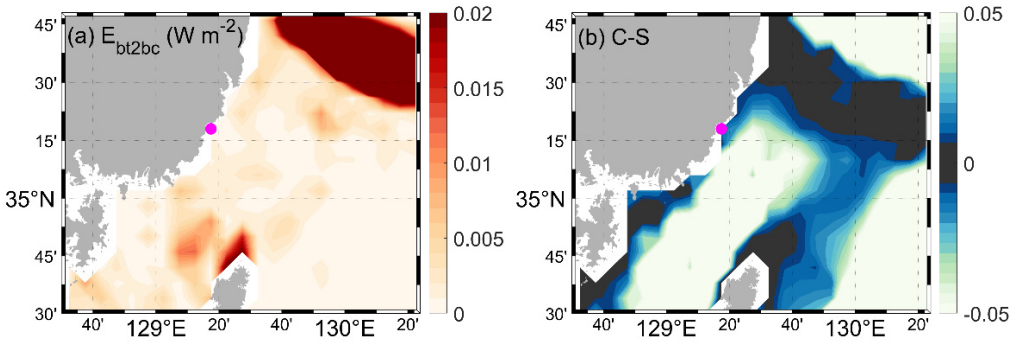

Figure 6. (**a**) Monthly-averaged barotropic to baroclinic energy conversion rate of semidiurnal tides in July 2015; (**b**) difference between the monthly-averaged wave characteristic slope (*C*) of the M_2 internal tide and bottom slope (*S*) in July 2015. The magenta circle indicates the location of the ADCP mooring site.

Favorable conditions for the generation of internal tides are achieved when the bottom slope (*S*) matches to the wave characteristic slope ($C = \pm\left[\left(\omega^2 - f^2\right)/\left(N^2 - \omega^2\right)\right]^{1/2}$) e.g., [8,20]. With matching slopes, the cross-shelf alignment of the tidal ellipse is important

for the generation of internal tides [21]. The difference between the monthly averaged C and S ($C-S$) for the M_2 frequency is almost zero at Northern Tsushima Island and the southern slope of the Ulleung Basin, which is consistent with the regions featuring high E_{bt2bc} (Figure 6b). Although the $C-S$ near the southeastern coast is also close to zero, internal tides could not be generated since a large part of the barotropic tide flows along the direction of the slope. Based on the map of E_{bt2bc} and $C-S$, we can conclude that semidiurnal internal tides cannot be locally generated near the southeastern coast of Korea. Therefore, observed variations in semidiurnal internal tides near the southeastern coast are presumed to be caused by the modification of their energy during their propagation from the generation region to the observation site (far-field process).

3.4. Propagation of Semidiurnal Internal Tides

Depth-integrated semidiurnal TE and EF averaged for July 2015 show highly relevant features in regions where E_{bt2bc} is high and $C-S$ is almost zero (Figure 7a). The semidiurnal internal tides generated at the southern slope of the Ulleung Basin do not propagate southward toward the mooring site; instead, they travel northeastward, in the direction of the energy flux. This result agrees well with that of Jeon et al. [14], who explained the characteristics of semidiurnal internal tides using the real-time forecast system of the East/Japan Sea.

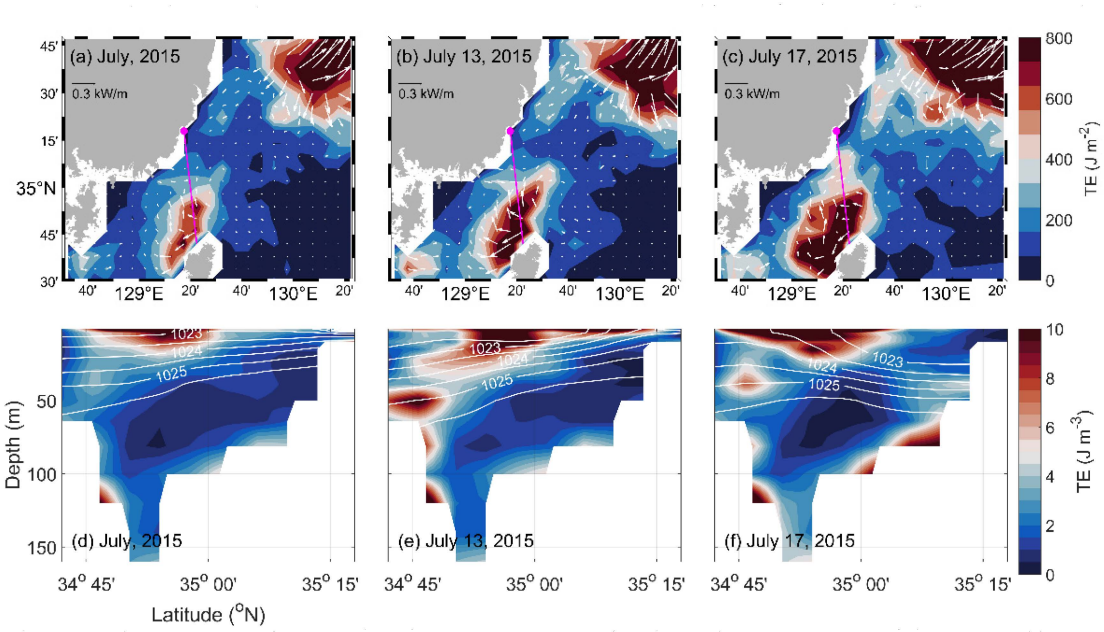

Figure 7. Average depth-integrated total energy (TE) and depth-integrated horizontal energy flux (EF) (arrows) for semidiurnal internal tides (**a**) in July, (**b**) on 13 July, and (**c**) on 17 July 2015; the vertical section of the average TE and density (white contour) (**d**) in July, (**e**) on 13 July, and (**f**) on 17 July 2015, along the magenta line in (**a**–**c**).

Apart from the Ulleung Basin, significant depth-integrated TE exists south of the mooring site. The depth-integrated TE extended from Northern Tsushima Island distributes close to the mooring site, and the EF directs northward. This pattern agrees well with the results of Lee et al. [9]. To observe the spatial energy patterns during typhoon-induced upwelling and downwelling, daily depth-integrated TE and EF are presented in Figure 7b,c. Overall, higher energy is noted for 17 July as the downwelling period overlaps with a spring tide. Notably, contrary to the observed results indicating that energy decreased during the upwelling period, the high TE seemingly approached the southeastern coast during the downwelling event.

The vertical distribution of the TE and density following the line from Northern Tsushima Island to the mooring site were investigated. The monthly mean vertical section for July 2015 shows that the pycnocline is tilted upward and remains near the southeastern

coast, and the TE continues from Tsushima Island (Figure 7d). On 14 July, during the upwelling period, the tilting of the pycnocline was enhanced, and the TE increased near the coast. However, on 17 July, when the downwelling event occurred, the pycnocline deepened, eliminating a stratification condition near the coast. Correspondingly, the semidiurnal internal tides do not come near the coast but converge on the bottom slope near the southeastern coast.

The wave reflection condition can explain the convergence of internal tides near the bottom slope. When a beam of semidiurnal internal tidal energy encounters the bottom, the beam is reflected with a certain amount of energy loss. The wave reflection condition is affected by stratification changes, which can be represented by the ratio between the C and S [22]. As shown in Figure 8, when S is steeper than C, the energy of the internal tides cannot be transmitted toward the coast and is reflected seaward. If both slopes are nearly equal, the wave is trapped near the bottom, leading to energy dissipation due to the turbulent movement. When C is steeper than S, the internal tidal energy can propagate landward.

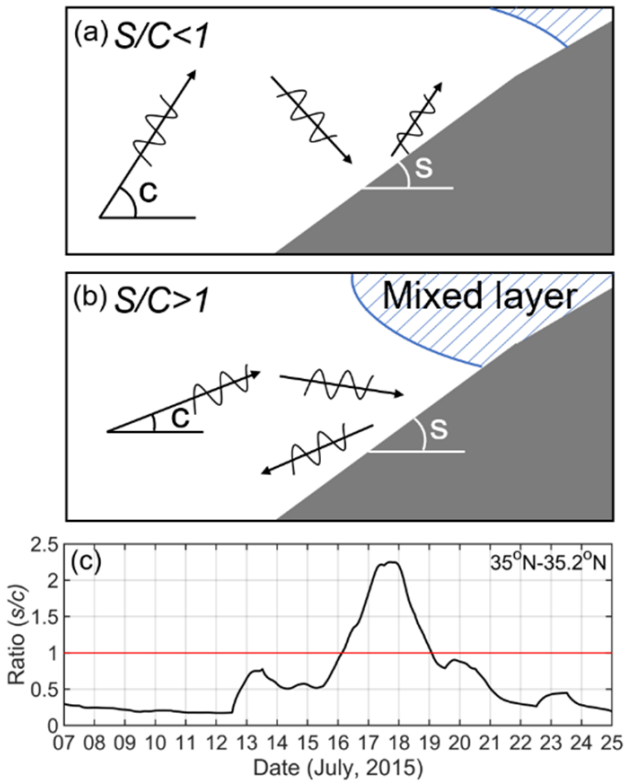

Figure 8. Schematic diagrams for reflection conditions (**a**) when the energy of internal tides can be transmitted to the coast ($S/C < 1$) and (**b**) when it can be reflected seaward ($S/C > 1$). (**c**) S/C ratio calculated using DR_M outputs by averaging between 35° N and 35.2° N along the magenta line in Figure 7.

The S/C ratio was calculated using the stratification conditions from the DR_M output and the slope from 35.0° N to 35.2° N, where the semidiurnal internal tidal energy is higher near the bottom (Figure 7f). The timeseries of the ratio (Figure 8c) reveals that C becomes gentle (less steep) during 16–18 July, when stratification is enhanced above the bottom due to the deepened pycnocline in the adjacent area. This creates a condition for the seaward reflection of semidiurnal internal tides ($S/C > 1$). In the other periods, the semidiurnal internal tides propagate landward. This result accounts well for the variation in semidiurnal internal tides observed by the ADCP and the simulated convergence process.

4. Conclusions

In July 2015, coastal upwelling and downwelling events caused by two typhoons occurred along the southeastern coast of the Korean Peninsula. Coincidentally, the energy of semidiurnal internal tides near the coast varied depending on the typhoon-induced stratification changes. The DR_M outputs show that the internal tidal signals could exist near the coast as they propagated from Northern Tsushima Island to the southeastern coast along the upward tilted pycnocline. However, during the downwelling event with deepened and flattened pycnocline near the coast, the internal tidal signal was considerably low and was independent of the barotropic tidal forcing. The vertical energy distribution also differed from that in the upward tilted pycnocline case, with the converged internal tidal energy on the bottom slope near the southeastern coast. This vertical energy distribution can be explained by the reflection condition, which depends on the ratio between the wave characteristic slope (C) and the bottom slope (S). The downwelling event creates conditions where the energy of internal tides is either trapped at the bottom or reflected seaward.

Typhoons frequently occur in the Northwestern Pacific, mainly during the summer. These strong cyclonic winds can create various phenomena near the coast with periods longer than a day, thereby modifying the typical stratification conditions. This study shows that typhoon-induced abrupt stratification changes can modify the propagation of semidiurnal internal tides. DR_M, the data-assimilated numerical model including tides, realistically simulated the interaction between semidiurnal internal tides and stratification changes. As internal tides play an important role in ocean mixing processes and can result in short-term environmental changes, our results provide insight for better understandings of the physical and biogeochemical processes associated with abrupt changes of internal tide energy along the southeast coast of Korea.

Author Contributions: J.-Y.C. analyzed the observation data and prepared the manuscript. C.J. and J.-H.P. took part in the preparation and editing of the manuscript. P.K. contributed by field experiment and data collection. N.H. ran the numerical simulation. A.K. took a part in the visualization. All authors have read and agreed to the published version of the manuscript.

Funding: This study was supported by "Study on air-sea interaction and process of rapidly intensifying typhoon in the Northwestern Pacific" funded by the Ministry of Ocean and Fisheries, Korea.

Institutional Review Board Statement: Not applicable.

Informed Consent Statement: Not applicable.

Data Availability Statement: The data presented in this study are available on request from the corresponding author.

Conflicts of Interest: The authors declare no conflict of interest.

References

1. Lee, J.-C.; Na, J.-Y. Structure of Upwelling off the Southease Coast of Korea. *J. Korean Soc. Oceanogr.* **1985**, *20*, 6–19.
2. Lee, J.C.; Kim, D.H.; Kim, J.-C. Observations of coastal upwelling at Ulsan in summer 1997. *J. Korean Soc. Oceanogr.* **2003**, *38*, 122–134.
3. Kim, S.-W.; Lim, J.-W.; Lee, Y.; Yamada, K. Response of Water Temperature in Korean Waters Caused by the Passage of Typhoons. *J. Korean Soc. Mar. Environ. Saf.* **2016**, *22*, 508–520. [CrossRef]
4. Kim, S.-W.; Go, W.-J.; Kim, S.-S.; Jeong, H.-D.; Yamada, K. Characteristics of ocean environment before and after coastal upwelling in the southeastern part of Korean Peninsula using an in-situ and multi-satellite data. *J. Korean Soc. Mar. Environ. Saf.* **2010**, *16*, 345–352.
5. Seo, H.-S.; Lim, W.-H.; Kim, D.-S. Numerical Experiments of Coastal Upwelling Occurred by Summer Winds in the East Sea of Korea. *J. Korean Soc. Mar. Environ. Saf.* **2017**, *23*, 347–353. [CrossRef]
6. Donaldson, M.R.; Cooke, S.J.; Patterson, D.A.; Macdonald, J.S. Cold shock and fish. *J. Fish Biol.* **2008**, *73*, 1491–1530. [CrossRef]
7. Attia, S.I. The influence of condenser cooling water temperature on the thermal efficiency of a nuclear power plant. *Ann. Nucl. Energy* **2015**, *80*, 371–378. [CrossRef]
8. Park, J.-H.; Watts, D.R. Internal Tides in the Southwestern Japan/East Sea. *J. Phys. Oceanogr.* **2006**, *36*, 22–34. [CrossRef]
9. Lee, H.J.; Lee, H.J.; Park, J.-H.; Ha, H.K. Seasonal Variability of Internal Tides around the Korea Strait: 3-D High-resolution Model Simulation. *Ocean Polar Res.* **2014**, *36*, 1–12. [CrossRef]

10. Hirose, N.; Takayama, K.; Moon, J.-H. Regional data assimilation system extended to the East Asian marginal seas. *Sea Sky* **2013**, *89*, 1–9.
11. Pawlowicz, R.; Beardsley, B.; Lentz, S. Classical tidal harmonic analysis including error estimates in MATLAB using T_TIDE. *Comput. Geosci.* **2002**, *28*, 929–937. [CrossRef]
12. Matsumoto, K.; Takanezawa, T.; Ooe, M. Ocean Tide Models Developed by Assimilating TOPEX/POSEIDON Altimeter Data into Hydrodynamical Model: A Global Model and a Regional Model around Japan. *J. Oceanogr.* **2000**, *56*, 567–581. [CrossRef]
13. Lee, H.J.; Park, J.-H.; Wimbush, M.; Jung, K.T.; Jang, C.J.; Cho, Y.-K.; Seo, Y.-K.; Nam, J.H. Tidal Effects on Intermediate Waters: A Case Study in the East/Japan Sea. *J. Phys. Oceanogr.* **2011**, *41*, 234–240. [CrossRef]
14. Jeon, C.; Park, J.-H.; Varlamov, S.M.; Yoon, J.-H.; Kim, Y.H.; Seo, S.; Park, Y.-G.; Min, H.S.; Lee, J.H.; Kim, C.-H. Seasonal variation of semidiurnal internal tides in the East/Japan Sea. *J. Geophys. Res. Ocean.* **2014**, *119*, 2843–2859. [CrossRef]
15. Chae, J.-Y.; Jeon, C.; Park, S.J.; Park, J.-H. Behavior of Diurnal Internal Waves in the Southwestern East/Japan Sea. *J. Coast. Res.* **2018**, *85*, 486–490. [CrossRef]
16. Zhao, Z.; Alford, M.H.; Lien, R.-C.; Gregg, M.C.; Carter, G.S. Internal Tides and Mixing in a Submarine Canyon with Time-Varying Stratification. *J. Phys. Oceanogr.* **2012**, *42*, 2121–2142. [CrossRef]
17. Park, J.-H.; Andres, M.; Martin, P.J.; Wimbush, M.; Watts, D.R. Second-mode internal tides in the East China Sea deduced from historical hydrocasts and a model. *Geophys. Res. Lett.* **2006**, *33*, L05602. [CrossRef]
18. Niwa, Y.; Hibiya, T. Three-dimensional numerical simulation of M 2 internal tides in the East China Sea. *J. Geophys. Res.* **2004**, *109*, C04027. [CrossRef]
19. Thomson, R.E.; Emery, W.J. *Data Analysis Methods in Physical Oceanography*, 3rd ed.; Elsevier: Oxford, UK, 2014; pp. 556–557. ISBN 978-0-12-387782-6.
20. Baines, P.G. On internal tide generation models. *Deep Sea Res. Part A. Oceanogr. Res. Pap.* **1982**, *29*, 307–338. [CrossRef]
21. Holloway, P.E.; Chatwin, P.G.; Craig, P. Internal Tide Observations from the Australian North West Shelf in Summer 1995. *J. Phys. Oceanogr.* **2001**, *31*, 1182–1199. [CrossRef]
22. Cacchione, D.A. The Shaping of Continental Slopes by Internal Tides. *Science* **2002**, *296*, 724–727. [CrossRef] [PubMed]